Additive Manufacturing 77 (2023) 103780

Contents lists available at ScienceDirect

Additive Manufacturing

journal homepage: www.elsevier.com/locate/addma

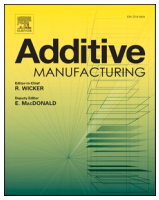

Research paper

The dependency chain in material extrusion additive manufacturing: Shaft torque, infeed load, melt pressure, and melt temperature

Austin R. Colon *, David O. Kazmer, Amy M. Peterson

Department of Plastics Engineering, University of Massachusetts Lowell, Lowell, MA 01854, USA

ARTICLE INFO

Keywords:
Material extrusion additive manufacturing
Fused deposition modeling
Fused filament fabrication
Rheology
Instrumentation

ABSTRACT

Current material extrusion systems can produce complex parts but lack instrumentation for observability and control. To investigate methods for observing the material extrusion process, a printer is instrumented to examine the dependency chain from the motor shaft torque to the infeed load and finally the melt pressure and temperature. The transient rheological and thermal behavior of the material extrusion process and the effect of volumetric flow rate, nozzle orifice diameter, and temperature setpoint on the pressure estimate from each point in the dependency chain are reported. The work also presents pressure predictions from COMSOL Multiphysics non-isothermal flow simulations and an analytical (Poiseuille) model. The pressure estimated by the motor shaft torque is greater than the downstream pressure estimated by the infeed load, which is greater than the downstream melt pressure in the hot end. In other words, both the torque sensor and the infeed load significantly overpredict the melt pressure. Significant variations in the pressures are also observed and explained. The findings demonstrate low and high frequency variation in the process, which can be attributed to gear eccentricity and teeth-to-filament engagement. The melt pressure variation is also observed to increase significantly at lower temperature set-points and higher flow rates, both of which reduce the melt temperature and thereby increase the viscosity. The increase in viscosity tends to reduce the viscous damping such that the variations in the filament infeed are transmitted through the hot end to the extrudate.

1. Introduction

Material extrusion additive manufacturing of thermoplastics is performed via an extrusion system mounted to a computer-controlled gantry, with the extrusion system typically comprised of a stepper motor, drive gear assembly, and hot end [1]. The stepper motor pushes the feedstock, in the form of a filament, into the hot end where it melts and passes through a nozzle orifice for deposition. This system design enables a variety of materials to be processed, using the driven feedstock to generate its own extrusion pressure, thereby providing users with design flexibility [2]. As an additive process, material extrusion also allows for designs of greater geometric complexity, relative to traditional manufacturing techniques [3]. Additionally, this type of additive manufacturing provides enhanced complexity at a low-cost, in comparison to other types of additive manufacturing [3]. Because of these advantages, this process sees application in a variety of industries, ranging from medical devices to unmanned air vehicles [4,5].

Despite its popularity, there are issues with the process, such as anisotropic mechanical properties [6] and processing artifacts such as voids and under-extrusion that result in stress concentrators [7]. There is also a lack of process observability, with most desktop systems providing only one sensor for the hot end temperature and another for the heated bed (if there is a heated bed). This lack of observability causes a lack of control over the rheological state of the material in the process related to the non-isothermal and transient flow in the hot end [8–10]. Additional sensors would enable inline rheological property characterization [11–15], part property prediction [16,17], process modeling [18], and advanced control strategies [19].

In the literature, there are instances of instrumentation for rheological monitoring in material extrusion. Approaches include monitoring the motor current [20], infeed load sensing via mounting the cold and hot end to a load cell [21–25], and placing a sensor in the nozzle to measure the pressure directly [26,27]. One work shows an example of a printer instrumented to measure motor current for the purposes of nozzle clog detection [28]. Serdeczny et al. report an infeed load sensor implemented to characterize the pressure required to extrude at different process conditions [22]. The work of Coogan and Kazmer uses a direct melt pressure measurement via a load column conveying the

* Correspondence to: University of Massachusetts Lowell, 220 Pawtucket St, Lowell, MA 01854, USA.
E-mail address: Austincolon97@gmail.com (A.R. Colon).

https://doi.org/10.1016/j.addma.2023.103780
Received 27 April 2023; Received in revised form 18 July 2023; Accepted 11 September 2023
Available online 14 September 2023
2214-8604/© 2023 Elsevier B.V. All rights reserved.

pressure from the melt to a beam-style load cell [26]. To date, there are no reports in the literature investigating the shaft torque of the extruder stepper motor as a means for rheological monitoring. Alternative techniques for in-situ monitoring include piezoelectric sensors for nozzle contact detection [29], infrared thermography [30,31], vibration sensors mounted to the print bed [32], and laser scanning technology [33], to name a few.

Modeling efforts of rheology in material extrusion additive manufacturing range from analytical models to numerical finite element simulations. The work of Bellini et al. [34] is well-known for providing a solution that predicts the pressure drop along the length of the material extrusion nozzle. Other analytical solutions have been implemented based on the Bellini model or other approaches [35–40]. There are also a variety of numerical simulations [18,19,41–47]. The modeling assumptions vary. Common material constitutive models include Newtonian, generalized Newtonian fluid, and viscoelastic [18,36]. Some models assume isothermal flow [35] while others do not [46]. Where the melting occurs in the nozzle also varies between the models; for example, Osswald et al. assume that melting occurs in the contraction of the nozzle, while Serdeczny et al. assume melting occurs as the thermoplastic enters the nozzle. The thermal properties vary as a function of temperature in some simulations [18,41]. Additionally, some models include the thermal contact resistance between the processed material and the wall of the nozzle while others do not [18]. Some simulations are validated against experimental data gathered via open extrusions over the print bed [42,46], while others have shown use in process control [19]. In most models, the nozzle flow bore has a circular cross section.

This work presents an experimental apparatus equipped to concurrently measure the motor shaft torque, infeed load, melt pressure, and melt temperature in a custom hot end. The advantages and disadvantages of each sensing technique are listed in Table 1. Combined, the sensor measurements enable characterization of the pressure dependency chain. This work investigates how pressure estimates vary depending on the monitoring technique, and how different process parameters affect the dependency chain. The instrumented printer also possesses an infrared (IR) array that enables melt temperature monitoring. The results show the effect of process variables on the measured melt temperature in a custom hot end.

2. Methodology

2.1. Filament selection and characterization

For these experiments, an acrylonitrile butadiene styrene filament (Hatchbox ABS, black) with a diameter of 1.75 mm is used. The material has a recommended processing temperature range of 210–240 °C. ABS is used because it is a popular material in both practice and research [48]. Following ASTM D3835–16, the filament was characterized using a capillary rheometer. Three temperatures and two die length to diameter ratios were used to enable correction of the apparent data and model fitting. The viscosity model selected is a power-law model with temperature dependency [49], as follows:

$$\eta(\dot{\gamma}, T) = k\dot{\gamma}^{n-1} \tag{1}$$

where η is the viscosity, $\dot{\gamma}$ is the shear rate, T is the temperature, and n is the power law index. In this form of the power-law model, the consistency index, k, incorporates temperature dependence via this equation:

$$k(T) = k_0 \exp(-A(T - T_{ref})) \tag{2}$$

where k_0 is the consistency index at the reference temperature, A is the temperature sensitivity parameter and T_{ref} is the reference temperature. The values for the coefficients fitted in MATLAB (Mathworks, Natick, MA) are shown in Table 2.

Fig. 1 shows the shear viscosity versus the shear rate (the value at the wall) as well as the pressure drop for a typical nozzle orifice (0.40 mm diameter and 0.40 mm length) versus the volumetric flow rate. The abscissas of the top and bottom figures are aligned so that the volumetric flow rate and shear rate correspond for a 0.40 mm nozzle orifice diameter. The pressure drop was calculated using Poiseuille's law [50]:

$$\Delta p = \frac{8\eta Q L}{\pi R^4} \tag{3}$$

where Δp is the pressure drop, Q is the volumetric flow rate, L is the length of the orifice bore, and R is the radius of the orifice bore. Fig. 1 shows that the viscosity decreases as the shear rate and temperature increase, demonstrating the pseudoplastic behavior of ABS and the dependence of viscosity on temperature. The pressure drop across the nozzle orifice increases as a function of flow rate and decrease as a function of temperature.

2.2. Experimental hardware

For the experimental apparatus (see Fig. 2), a Creality (Shenzhen, China) Ender 5 Pro is adapted. The stock extruder is replaced with a Micro Swiss (Minneapolis, Minnesota) direct drive extruder, which is further modified to incorporate the 0.5 Nm torque sensor (Dongguan NanLi Co. Ltd., Guangdong, China) and the infeed and melt sensors (SparkFun Electronics, Niwot, CO, Part Number: SEN-14729, combined error of 0.05% of the full-scale value). An aluminide plate from i. Materialise (Leuven, Belgium) is used to mount the infeed and melt sensors as well as the IR array (HTPA32x32dR2-L5.0/0.85F7.7HiS, Heimann Sensor GMBH, Eltville, Germany). An aluminide bracket attaches the infeed sensor to the cooling block and downstream hot end. A timing belt and pulley system transmits the rotation of the stepper motor to the torque sensor's shaft. Details on data acquisition are included in supplementary materials section S.1.

The hot end is a custom design shown in Fig. 3 that is manufactured in bronze by i.Materialise using a casting process. The design is intended to enhance the melting of the thermoplastic by lofting the circular inlet having a diameter of 2 mm to a thin slit having a width of 3 mm and a thickness of 1 mm. The thinness of the slit increases the rate of heat transfer while the wideness of the slit enables the use of a larger diameter load pin to increase the signal-to-noise ratio for melt pressure measurement compared to Coogan and Kazmer [26]. The slit geometry

Table 1
Advantages and disadvantages of the investigated monitoring techniques.

Monitoring Technique	Advantage(s)	Disadvantage(s)
Motor torque	• Least invasive to process • High sensitivity	• Relatively large and expensive • Least reflective of states in nozzle
Infeed pressure	• Least expensive option • Closer to nozzle orifice than motor torque	• Farther from nozzle orifice than melt pressure
Melt pressure	• Direct measurement • High sensitivity	• Expensive, custom hardware • Most invasive to process
Infrared melt temperature	• Close to nozzle orifice • High sensitivity	• Expensive, custom hardware • Calibration required

Table 2
Temperature-dependent power-law model coefficients for ABS.

Coefficient	Value
n	0.3406
k_0 [Pa-s]	46679
A [°C^{-1}]	0.02197
T_{ref} [°C]	178.32

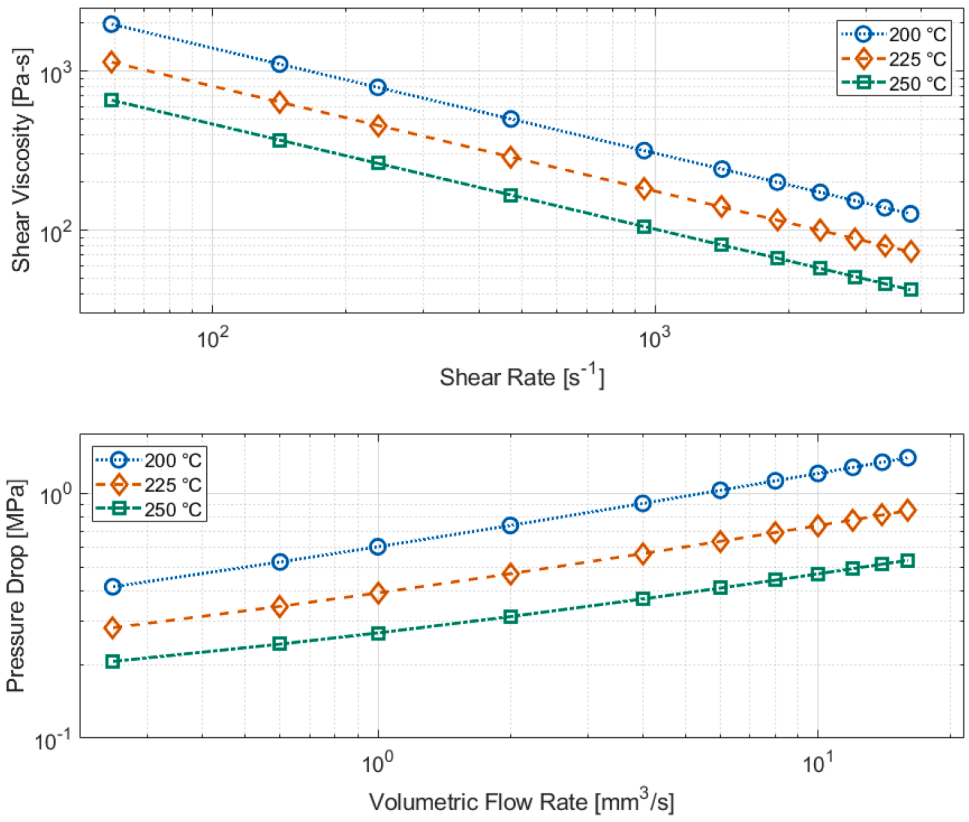

Fig. 1. Shear viscosity versus shear rate and estimate pressure drop versus volumetric flow rate for a nozzle orifice 0.40 mm in diameter and 0.40 mm long. The data points represent model values. For the shear viscosity, the model values are calculated with Eq. 1. The pressure drop is across the length of the nozzle orifice, calculated using Eq. 3.

also provides for the addition of a window opposing the load pin for viewing the melt. Here, a zinc selenide (ZnSe) lens is held in place by a set screw with a through-hole to provide a window for the infrared (IR) radiation from the melt to pass through to the IR array. Nozzles with varying orifice sizes are from McMaster-Carr (part numbers 3695N301, 3695N304, 3695N306, Elmhurst, IL, USA) and are made of brass. Two 40 W heater cartridges are used in the hot end to provide double the heating power of a typical hot end. A thermistor is used to control the temperature of the hot end. A pin with a diameter of 3.02 mm is used to transmit the applied stress from the melt in the hot end to the load cell. A nylon hex bolt provides a contact surface to transmit the resulting force to the load cell while minimizing heat transfer. Fig. 3 shows the typical nozzle design (3695N304) with a nozzle orifice diameter and length of 0.40 mm.

2.3. Experimental factors

To study the dependency chain in the material extrusion process, the volumetric flow rate, temperature setpoint, and the nozzle orifice diameter are varied one factor at a time. The volumetric flow rates used are 1 mm^3/s, 5 mm^3/s, and 10 mm^3/s. These volumetric flow rates are based on common print speed values used in the material extrusion process and correspond to road widths 0.05 mm larger than the nozzle diameter and a road height of 0.20 mm [22,51,52]. The temperature setpoints used are 200 °C, 225 °C, and 250 °C, based on the recommended processing temperature range for the ABS filament. To study the effect of nozzle orifice diameter, nozzles with orifice diameters of 0.25 mm, 0.40 mm, and 0.60 mm are used. All three nozzle orifices have a length equal to their diameter. The most common nozzle diameter used in desktop material extrusion systems is 0.40 mm [1,45,53]. The other two diameters are selected to bracket that value. There are a total of seven unique runs, as shown in Table 3.

The test procedure begins by allowing the hot end temperature to equilibrate for 2 min before each unique run is performed. Then, a creeping flow of 0.6 mm^3/s is maintained for two minutes to ensure a steady process without material degradation. The process then dwells without filament retraction. The material is then extruded approximately 75 mm above the print bed for three minutes. Throughout, the data acquisition system collects the data from the torque, infeed, and melt sensors, and the IR array collects images.

2.4. Analysis

The sensor voltages are collected by the data acquisition system at a scan rate of 50 kHz and multiplied by a gain value determined by a calibration experiment using known loads. The infeed and melt sensors produce force readings when multiplied by their gains, while the torque sensor produces a torque value when multiplied by its gain. To estimate the melt pressure, the force on the melt load cell is divided by the cross-sectional area of the load pin. For the infeed pressure, the force measured by the load cell is divided by the cross-sectional area of the filament. For the torque sensor, the shaft torque is divided by the pitch radius of the gear, 3.875 mm, then divided by the cross-sectional area of the filament to get a drive pressure estimate.

The IR data is collected as a 32 by 32 grid of temperature across the field of view at a scan rate of 8 Hz. To analyze the IR images, the matrix of temperatures at each time step is imported into MATLAB as a text file. The images are first masked to focus the analysis on the ZnSe lens. Once the images are masked, the average voltage value across the remaining pixels is calculated. A quadratic equation is then used to convert the average voltage value to a temperature value. The quadratic equation is determined by a calibration experiment where the hot end is allowed to reach thermal equilibrium at known temperature values. For both the pressure data and the temperature data, the average and standard

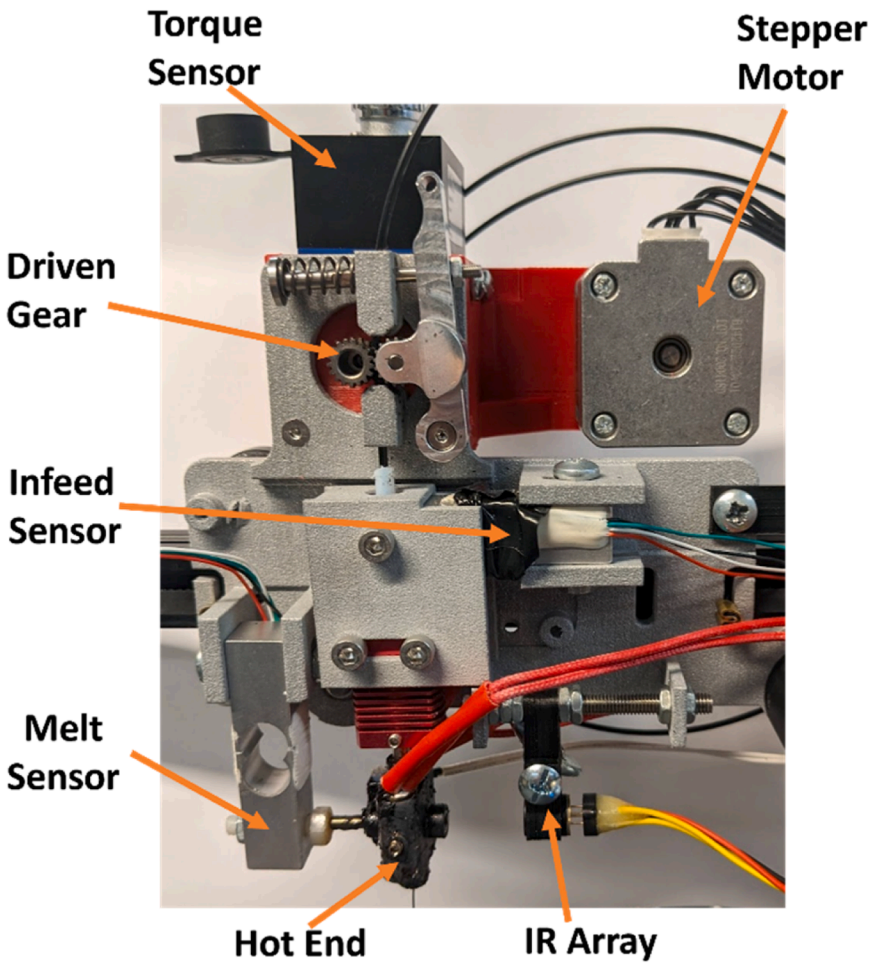

Fig. 2. The instrumented extrusion system.

deviation of temperature are calculated by using the last one hundred seconds of data during the extrusion.

3. Numerical Simulation and Analytical Modeling

3.1. General methodology and equations

The system is modeled in SolidWorks (Dassault Systemes, Vélizy-Villacoublay, France). The model is then imported into COMSOL Multiphysics (COMSOL, Inc., Burlington, MA, USA). The air around the hot end is modeled as a cylinder, with the volume of the hot end body, heat sink, PTFE tube, nozzle, heater cartridges, and thermoplastic removed. The components besides the air are modeled as their own domains. The thermoplastic is divided into a solid filament, the molten material in the hot end body and nozzle, and a solid extrudate. A non-isothermal flow simulation is used to model the material inside the hot end body and nozzle. The fluid flow of the air is not simulated, but convection is still accounted for and will be discussed later. To model the flow of the polymer, the three conservation equations for mass, momentum, and energy are considered at steady state [54]:

$$\nabla \bullet (\rho \boldsymbol{u}) = 0 \tag{4}$$

$$\rho(\boldsymbol{u} \bullet \nabla)\boldsymbol{u} = \nabla \bullet \left[-p\boldsymbol{I} + \mu\left(\nabla \boldsymbol{u} + (\nabla \boldsymbol{u})^{\mathrm{T}}\right) - \left(\frac{2}{3}\right)\mu(\nabla \bullet \boldsymbol{u})\boldsymbol{I} \right] \tag{5}$$

$$\rho C_p(\boldsymbol{u} \bullet \nabla T) + \nabla \bullet (-k\nabla \mathrm{T}) = \boldsymbol{\tau} : \nabla \boldsymbol{u} - \left(\frac{1}{\rho}\right)\left(\frac{\delta \rho}{\delta T}\right)T(\boldsymbol{u} \bullet \nabla p) \tag{6}$$

where ∇ is the gradient operator, $\rho$is the density, $\boldsymbol{u}$ is the velocity vector, p is the pressure, $\boldsymbol{I}$ is the identity matrix, μ is the dynamic viscosity, the superscript $\boldsymbol{T}$ indicates the transpose operation, C_p is the specific heat at constant pressure, T is the temperature, k is the thermal conductivity, and $\boldsymbol{\tau}$ is the viscous stress tensor. It should be noted that the flow is steady in a Eulerian sense, but not in a Lagrangian approach. The strain rate tensor is defined as:

$$\dot{\boldsymbol{\gamma}} = \left(\frac{1}{2}\right)(\nabla \boldsymbol{u} + (\nabla \boldsymbol{u})^T) \tag{7}$$

where $\dot{\boldsymbol{\gamma}}$ is the strain rate tensor. The shear rate is defined as the magnitude of the strain rate tensor:

$$\dot{\gamma} = \sqrt{2\dot{\boldsymbol{\gamma}} : \dot{\boldsymbol{\gamma}}} \tag{8}$$

For the thermoplastic, the viscous stress tensor is defined by Newton's law of viscosity:

$$\boldsymbol{\tau} = 2\mu\dot{\boldsymbol{\gamma}} \tag{9}$$

To calculate the dynamic viscosity, Eq. 2 is substituted into Eq. 1, and the resulting viscosity value is used. This equation is implemented in COMSOL for the material's viscosity by calculating the shear dependent portion of Eq. 1 using a piecewise function and calculating the temperature dependent portion from Eq. 2 as an analytical function; the product of the resulting values gives the desired viscosity. In the solid domains and the air, only the energy conservation equation is considered, for heat transfer purposes. The terms for viscous heating and pressure work are not included when the energy equation is

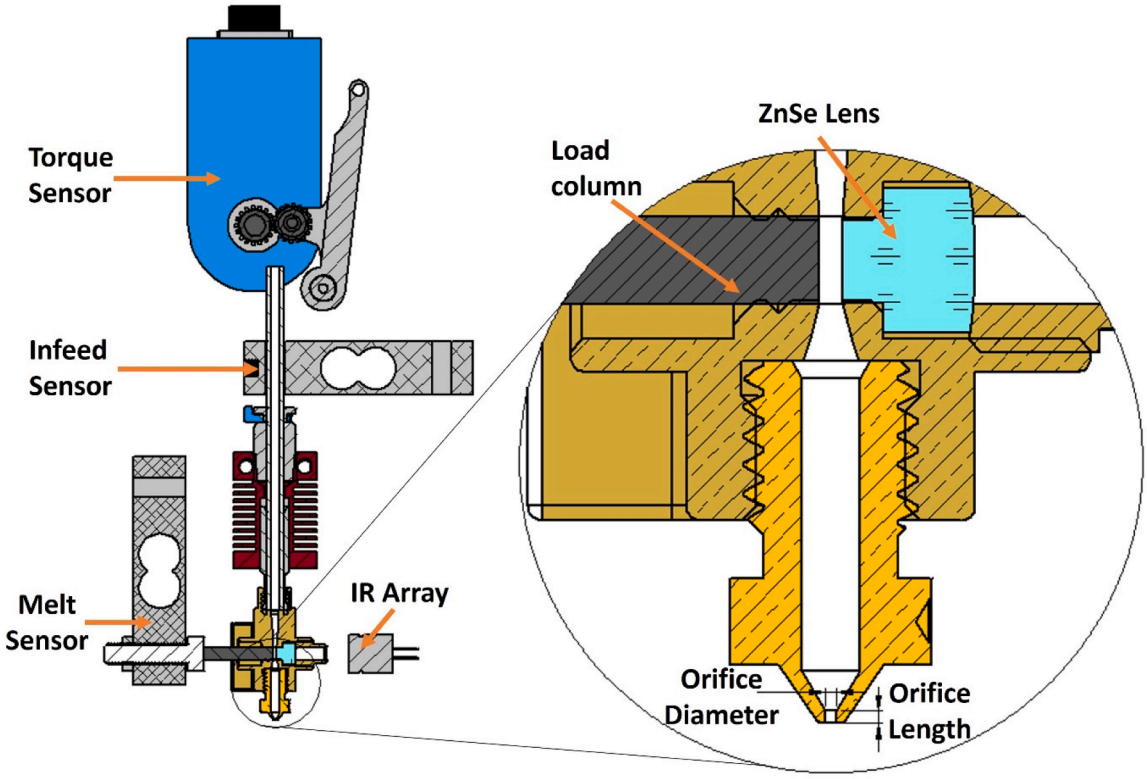

Fig. 3. A cross-sectional view of the custom hot end, showing how a load column transfers the pressure from the melt to a load cell, as well as the ZnSe lens.

Table 3
Implemented design of experiments.

Run (description)	Volumetric Flow Rate [mm^3/s]	Temperature [°C]	Nozzle Diameter [mm]
1 (center point)	5	225	0.4
2 (low flow rate)	1	225	0.4
3 (high flow rate)	10	225	0.4
4 (low temperature)	5	200	0.4
5 (high temperature)	5	250	0.4
6 (small orifice)	5	225	0.25
7 (large orifice)	5	225	0.60

implemented in these domains. Convection is accounted for in the air domain via calculation of a Nusselt number applied to the conduction term of the energy equation, resulting in convectively-enhanced conduction.

3.2. Assumptions and boundary conditions

For the thermoplastic, the flow is assumed to be compressible, non-Newtonian (shear thinning), non-isothermal (temperature-dependent viscosity), laminar, and at steady state. A no-slip boundary condition is assumed at the wall. The inlet condition at the entrance of the hot end body with a constant velocity profile is prescribed by a user-defined volumetric flow rate and the outlet pressure is defined as atmospheric pressure of 101,325 Pa. The density, specific heat, and thermal conductivity of the thermoplastic are assumed to vary with temperature. Also, viscous dissipation is assumed to occur within the melt [55].

For the brass, bronze, stainless steel, and PTFE components, their thermal conductivity, specific heat, and density are assumed constant. The air properties are modeled as a function of temperature and there is convective heat transfer governed by a user defined Nusselt number [56] as mentioned previously. Details on the material properties for the solid phases and air are presented in supplementary materials section S.2 and calculation of the Nusselt number is included in supplementary materials S.3.

To model the ambient temperature around the system, a temperature condition is defined on the outer surface of the cylinder surrounding the hot end. To simulate the thermistor being at temperature, the temperature is set as the temperature setpoint on the boundaries of the thermistor port. A heat source boundary condition is used to simulate the heater cartridges providing power to heat the system, with a heat rate value of 80 W, distributed across the surface of the heater cartridge domains. Contact resistance between the melt and hot end and between the hot end threads and the threads of the nozzle is modeled in this simulation, similar to contact resistance in an injection mold [57]. Details on contact resistance modeling are in supplemental materials section S.4.

3.3. Meshing

The modeled melt has a finer mesh than the rest of the model because computational fluid dynamics (CFD) requires a fine mesh to be accurate. Specifications on the size of the mesh are included in supplementary materials section S.5. A sensitivity analysis is performed to ensure the mesh is appropriate. The average mesh size in the melt and extrudate domains was refined from 0.288 mm to 0.226 mm with a 0.045% change in behavior, which indicates the mesh effects are minimal. Fig. 4 shows the mesh, as well as some of the boundary conditions implemented in the model.

3.4. Analytical Model

In addition to the numerical simulation, the Poiseuille equation (Eq. 3) is used to calculate the pressure drop. The pressure drop between the

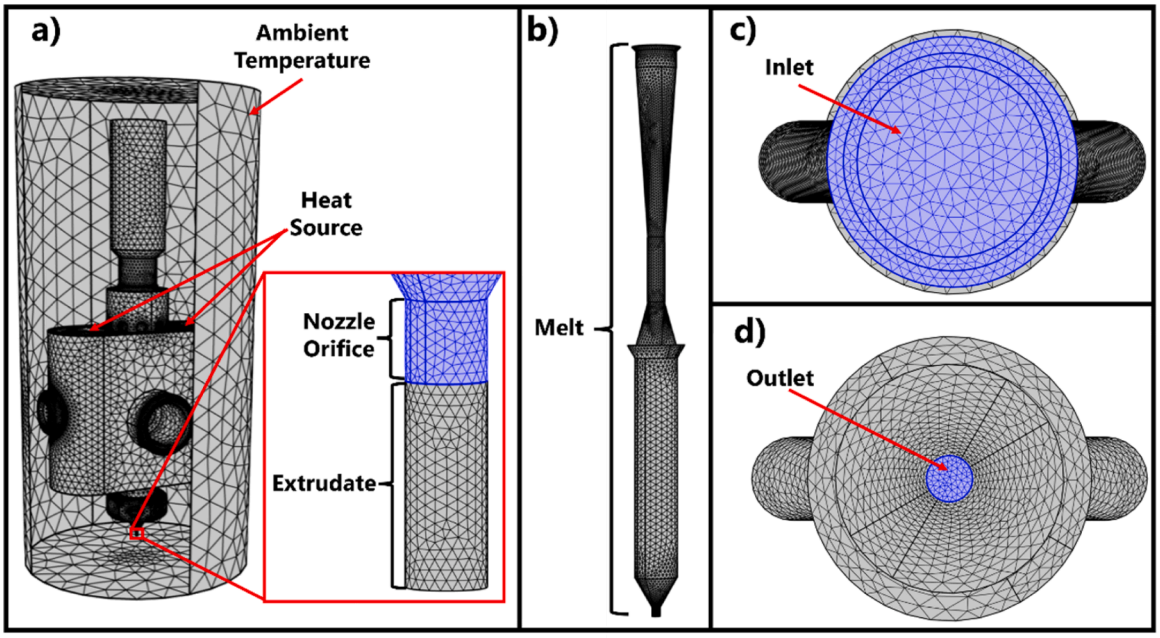

Fig. 4. Model mesh of a) the overall geometry, b) the melt alone, c) the inlet, and d) the outlet.

load pin and the nozzle orifice is estimated as the sum of the pressure drops in the lower half of the slit (assuming an equivalent hydraulic diameter), the nozzle entrance bore, and the nozzle orifice. The minor losses were calculated using the following equation [56]:

$$\Delta p = \frac{K_L \rho V^2}{2} \tag{10}$$

where K_L is the loss coefficient and V is the flow velocity in the tube with the smaller diameter. The values of K_L depend on the geometry of the contraction or expansion [56]. Going down the length of the hot end flow bore, the minor losses are calculated as follows:

1. The loft from the slit geometry to the circular flow bore is considered a gradual expansion with a loss coefficient value of 0.121. This loss coefficient is calculated by using linear interpolation between values of 0.15 and 0.10 given for an included expansion angle of 20° with diameter ratios of 0.6 and 0.8, respectively [56]. The diameter ratio for the gradual expansion from the slit to the loft is 0.715, since the hydraulic diameter of the slit is 1.36 mm and the diameter of the circular cross section at the end of the hot end flow bore has a diameter of 1.9 mm.
2. A sudden expansion from the diameter of the hot end body's circular flow bore to the nozzle entrance bore diameter has a loss coefficient of 0.019, since the diameters are close with the circular cross-section at the end of the hot end body being 1.9 mm and the nozzle entrance bore diameter being 2.0 mm. The equation used to calculate this calculate this K_L is as follows [56]:

$$K_L = \alpha(1 - \frac{d^2}{D^2})^2 \tag{11}$$

   where α is equal to 2 for fully developed laminar flow, d is equal to the pipe diameter prior to the expansion, and is equal to the diameter after the expansion.
3. The K_L for a contraction with an included angle of 60° is 0.07 [56]. Typical pressure losses due to the contraction from the entrance bore diameter to the nozzle orifice diameter are on the order of 0.38 Pa, 0.060 Pa, and 0.011 Pa for 0.25 mm, 0.40 mm, and 0.60 mm nozzle orifice diameters, respectively, at a volumetric flow rate of 5 mm^3/s and assuming the density of ABS is 1042 kg/m^3.

A diagram is provided in supplementary materials section S.6 that indicates where these minor losses occur in the hot end.

4. Results

Transient pressure plots of the three different sensor measurements are shown in Fig. 5. Each subplot is for a different experiment volumetric flow rate with the same nozzle orifice diameter of 0.40 mm and temperature setpoint of 225 °C. The torque sensor always provides a pressure estimate greater than the other two sensors, and the infeed sensor pressure is always greater than the melt pressure measurement. All three sensors show that the pressure increases with the volumetric flow rate. After the creeping flow concludes, the torque sensor reading does not return to zero, indicating that there is strain retained within the torque sensor that is not relieved when the gear stops rotating.

The torque sensor measurements show the most variation over time, followed by the infeed sensor and then the melt sensor. This variation is not noise, but rather has low and high frequency components related to the eccentricity of the gears on the shaft and the individual burs biting into the filament as later discussed. These torque variations are indicative of transient compressive stresses applied to the filament that are transmitted to the infeed load sensor and melt pressure sensor. The speed of sound in the material is $v = \sqrt{\frac{E}{\rho}} \sim 1000$ m/s with a modulus, E, around 1 GPa and density, ρ, around 1000 kg/m^3. Accordingly, no significant phase lag is expected given the short distances, while damping is observed given viscous dissipation.

With the imposed experimental flow rates, the maximum pressure of 7 MPa is observed at the torque sensor with the 10 mm^3/s volumetric flow rate, while the minimum pressure of 0.80 MPa is observed at the melt sensor with the 1 mm^3/s volumetric flow rate. The pressure also tends to overshoot at the start of the experimental extrusion. Similar overshoots in the pressure, or feeding force, are seen at the start of extrusion in other works [42]. This overshoot is believed to be due to cooler nozzle material temperatures at the start of extrusion, which then increase due to viscous dissipation and heat transfer from the heated material to the nozzle.

The transient pressure values for the three nozzle orifice diameters are shown for a volumetric flow rate of 5 mm^3/s and a temperature setpoint of 225 °C in Fig. 6. The torque sensor detects very similar loads

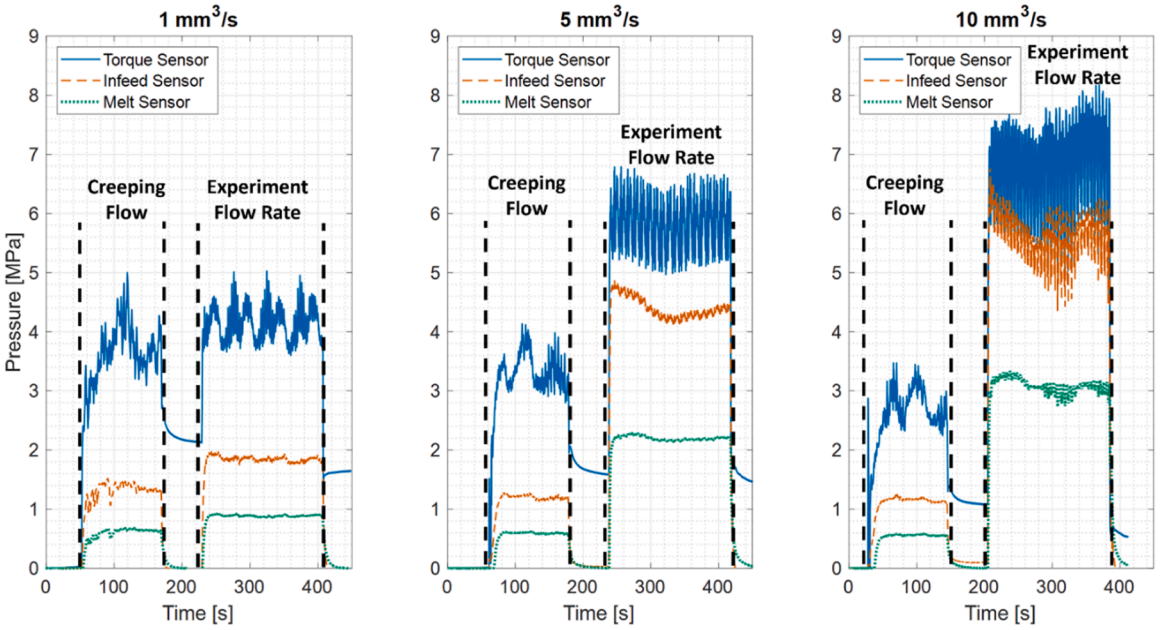

Fig. 5. Transient pressure data from the three sensors at three volumetric flow rates. The lefthand plot is for 1 mm^3/s, the middle plot is for 5 mm^3/s, and the righthand plot is for 10 mm^3/s. All the data was collected with a nozzle orifice diameter of 0.40 mm and a temperature setpoint of 225 °C.

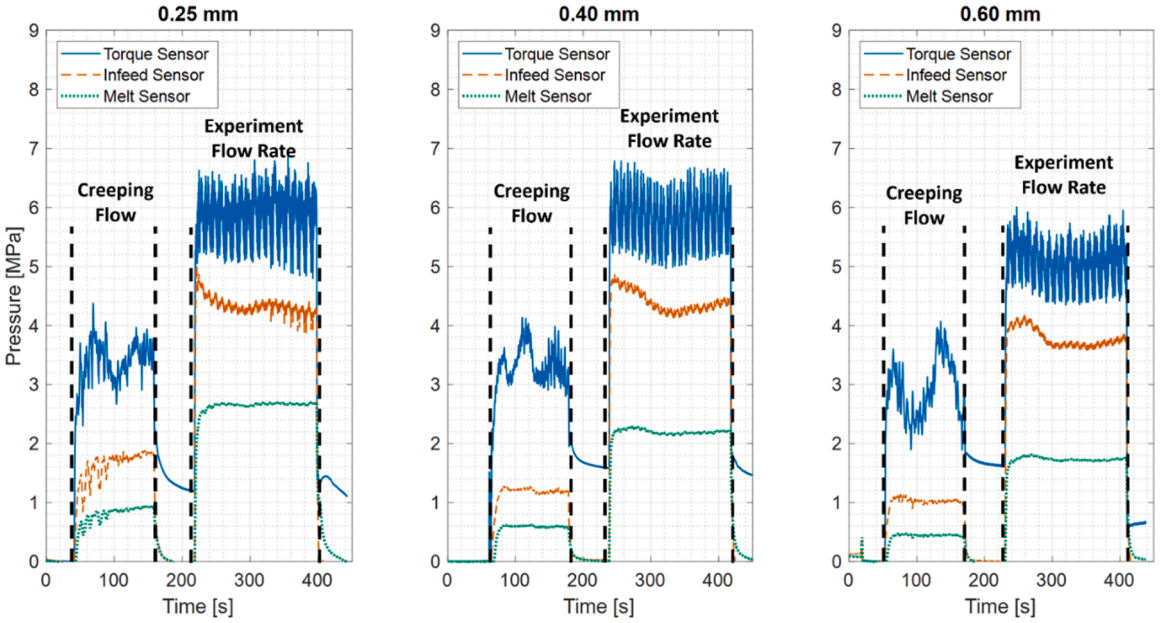

Fig. 6. Transient pressure data from the three sensors at three nozzle orifice diameters. The lefthand plot is for 0.25 mm, the middle plot is for 0.40 mm, and the righthand plot is for 0.60 mm. The data was collected at a temperature setpoint of 225 °C and a volumetric flow rate of 5 mm^3/s.

during extrusion for the 0.25 and 0.40 mm orifice diameters with a reduction in the load for the 0.60 mm nozzle orifice diameter. The infeed pressure exhibits a decrease from its initial value for all three nozzle orifice diameters, and similar behavior is seen in the melt pressure sensor. These behaviors are generally consistent with expectations based on the Poiseuille equation of Eq. (10), though the range of pressures is diminished by the shorter length of the nozzle bores.

The transient pressures for different temperature setpoints using the 0.40 mm nozzle orifice diameter and a volumetric flow rate of 5 mm^3/s are shown in Fig. 7. The data shows that the pressure decreases as a function of temperature setpoint for all three sensors. The variation in the pressure measurement also appears to decrease as a function of temperature setpoint. These two behaviors also follow expectations. First, the viscosity decreases with temperature per Eq. (2), which corresponds to the lower observed pressures. Second, elevated temperatures also increase the ratio of the loss to storage modulus, which accounts for the increased damping observed. In other words, the material has more solid-like behavior at lower temperatures and provides direct transmission of the applied stresses from the drive gear.

Fig. 8 shows the main effects for each steady state sensor response (average during the 180 s of experiment flow rate with error bars representing the standard deviation) as a function of each factor. All the results show that the average pressure decreases as the sensor location gets closer to the nozzle. For the left subplot of Fig. 8, where a 0.40 mm nozzle orifice diameter and temperature setpoint of 225 °C are used, the average pressure increases for all three sensors as a function of

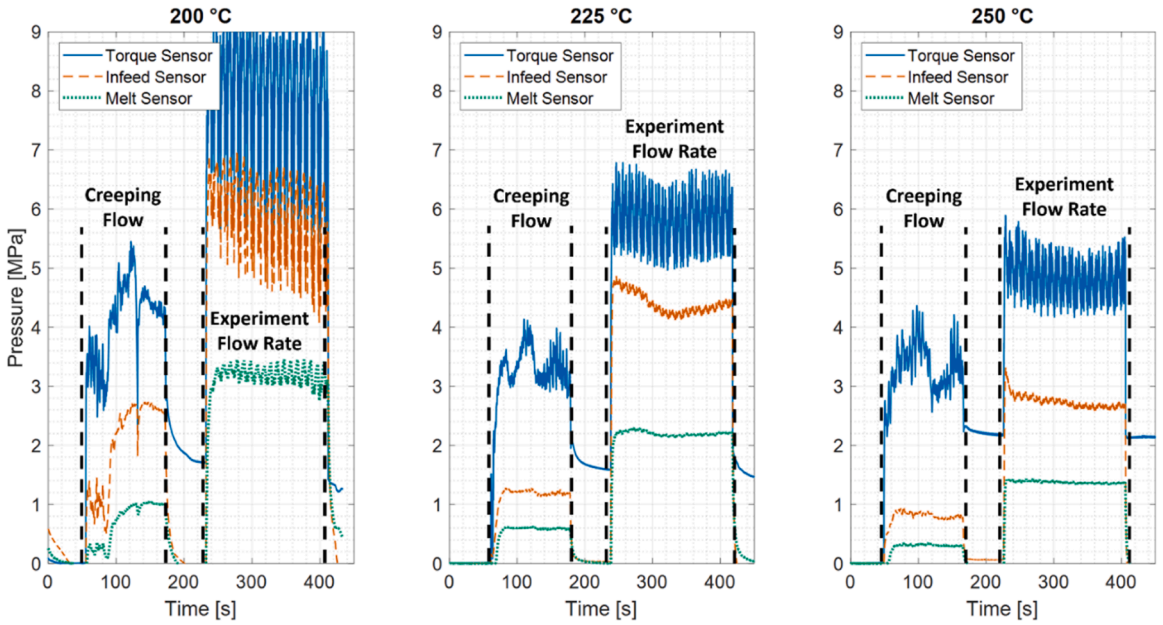

Fig. 7. Transient pressure data from the three sensors at three temperature setpoints. The lefthand plot is for 200 °C, the middle plot is for 225 °C, and the righthand plot is for 250 °C. All the data was collected with a nozzle diameter of 0.40 mm and a volumetric flow rate of 5 mm^3/s.

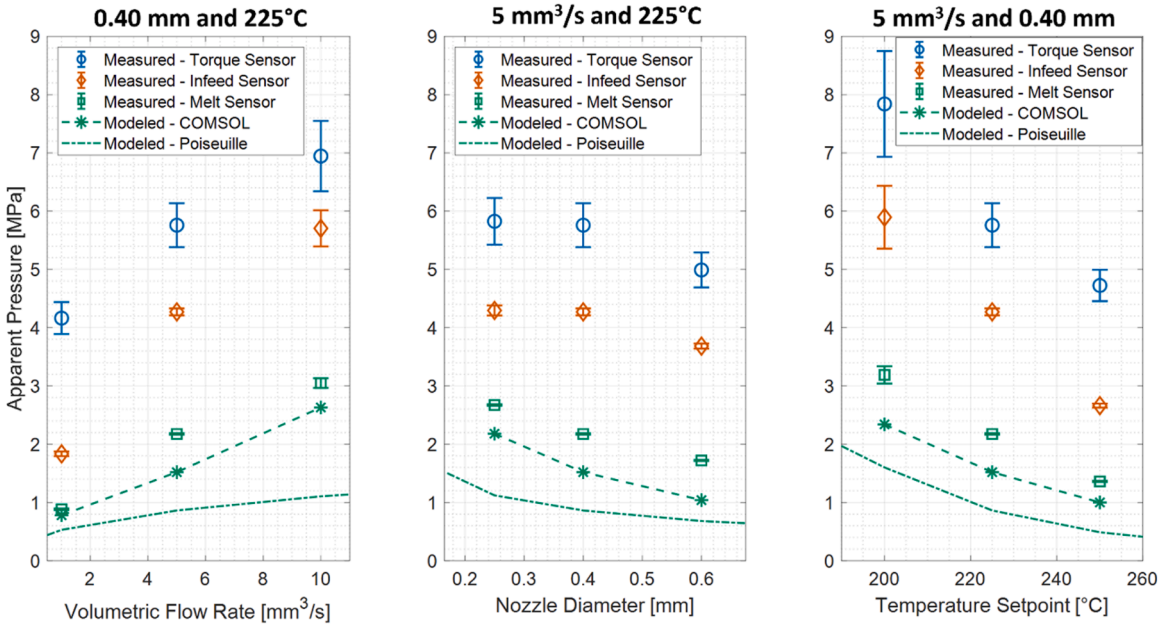

Fig. 8. Average measured pressure versus the factors for each sensor. The modeled pressure using COMSOL and the analytical Poiseuille equation are also shown. For the measured data, the data points are the average values and the error bars represent one standard deviation.

volumetric flow rate, as seen in the transient data. The error bars imply that the standard deviation for the torque sensor is greater than the other two sensors, and that the standard deviation tends to increase as a function of volumetric flow rate for all three sensors. The middle subplot of Fig. 8, where a temperature setpoint of 225 °C and volumetric flow rate of 5 mm^3/s are used, shows that the 0.60 mm nozzle orifice diameter has a lower pressure estimate than the other two nozzle orifice diameters, based on the torque sensor. The same is true for the infeed sensor. For the melt sensor, the average pressure more clearly decreases as a function of nozzle orifice diameter. The righthand plot of Fig. 8, where a 0.40 mm nozzle orifice diameter and a volumetric flow rate of 5 mm^3/s are used, shows the pressure as a function of the temperature setpoint and indicates that the standard deviation of the temperature decreases as a function of temperature setpoint. The low temperature setpoint and the high volumetric flow rate provide the highest pressures, while the low flow rate provides the lowest pressure.

Fig. 7 also plots the results of the numerical simulation and analytical model. For the COMSOL model, the trends in the modeled melt pressure generally agree with the experimental data, though the modeled values undershoot the experimental values across all conditions. The COMSOL model underpredicts the pressure drop because the experimental temperature of the material at the measurement port may be lower than the predicted temperature at that location in the simulation. This results in a higher viscosity and more pressure required for the material to flow. For comparison, the analytical Poiseuille equation and the minor losses were calculated from halfway down the slit to the bottom of the nozzle orifice.

The total pressure was then calculated by adding the estimated pressure loss to atmospheric pressure. One likely reason why the analytical model underpredicts the pressure more than the COMSOL model is because it assumes that the processed material is at a uniform temperature while the temperatures are known to vary based on experiments and COMSOL.

The measured pressure loss in the melt is shown as a function of each factor in Fig. 9 wherein the measured pressure loss is calculated as the difference between the infeed pressure and the melt pressure measurement. For the lefthand subplot, the pressure loss increases as a function of the volumetric flow rate. The standard deviation in the pressure loss also increases as a function of volumetric flow rate for reasons related to melt temperature as subsequently discussed. For the middle subplot, pressure losses are expected to be constant since the melt flow rate and temperature are constant. The results show that there is no clear trend in the pressure loss as a function of nozzle orifice diameter, though the pressure loss is slightly lower for the 0.25 mm nozzle orifice diameter than the other two sizes. For the righthand subplot, the pressure loss decreases as a function of temperature setpoint. The standard deviation of the pressure loss also decreases as a function of temperature setpoint. Both of these results are expected given the decreased viscosity as a function of increasing temperature.

Fig. 10 shows the temperature measured by the IR array as a function of time. The dashed vertical lines indicate when the experimental flow rate starts and ends. Each curve represents a different volumetric flow rate. As the volumetric flow rate increases, the temperature drop during extrusion increases, indicating non-isothermal conditions in the hot end. This plot also shows that there is an initial drop and slight recovery of the temperature over the course of about one minute for the 5 mm^3/s and 10 mm^3/s data sets. The 1 mm^3/s data set shows no decrease in the temperature during extrusion. Approximately 30 s into the experiment flow rate, temperature oscillations of 3 and 6 °C are observed for the 5 mm^3/s and 10 mm^3/s data, respectively. The initial decrease is likely due to the drawdown in temperature given the thermal mass of the hot end upon the increase in flow rates and related heat conveyance to the processed material. Some of the temperature drop is then restored upon further heating of the hot end by its closed loop controller, although a steady state error is observed. While the steady state error can be reduced by moving the feedback temperature sensor closer to the melt, the transient behavior is a significant concern given the frequent starting and stopping of the extruder during nozzle repositioning in the additive manufacturing.

Fig. 11 shows the average measured temperature values during the creeping flow phase of the experiment and the average temperature during the extrusion at the experimental flow rate. The lefthand plot shows the temperature as a function of volumetric flow rate, and indicates the observed trend from the transient data, with the 1 mm^3/s data points overlapping and the 10 mm^3/s temperature dropping to around 222 °C. As shown in the middle plot, the average temperature during creeping flow is observed to decrease as a function of nozzle diameter. The average temperature during the experiment flow rate also decreases. From the righthand plot, the temperature increases as a function of temperature setpoint.

The melt temperature at the creeping flow rate and experiment volumetric flow rate are plotted in Fig. 12. The lefthand subplot shows that the temperature decreases as the volumetric flow rate increases. The middle plot shows that the 0.40 mm nozzle is the only one that shows a decrease in the temperature upon extruding at the commanded volumetric flow rate for the same volumetric flow rate and temperature setpoint. The righthand subplot shows that the temperature decreases slightly more for the center and high temperature setpoints than the low temperature setpoint. Overall, the most significant factor is the experimental volumetric flow rate.

5. Discussion

For the transient measurements, increased pressure as a function of volumetric flow rate comports with expectations since the shear rate and shear stress will increase as a function of the volumetric flow rate. The pressure changes as a function of temperature and nozzle orifice diameter are also consistent with expectations. It also is reasonable that the

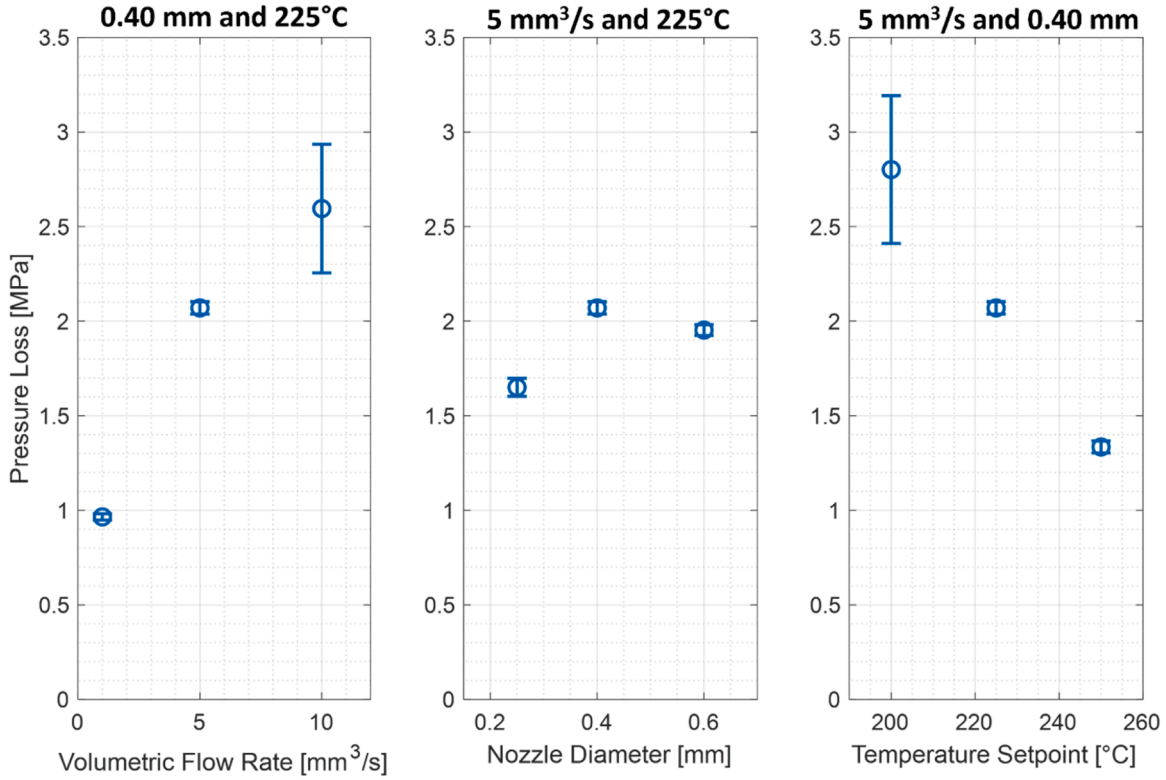

Fig. 9. Measured pressure loss in the melt versus the factors. The data points are average values and the error bars represent one standard deviation.

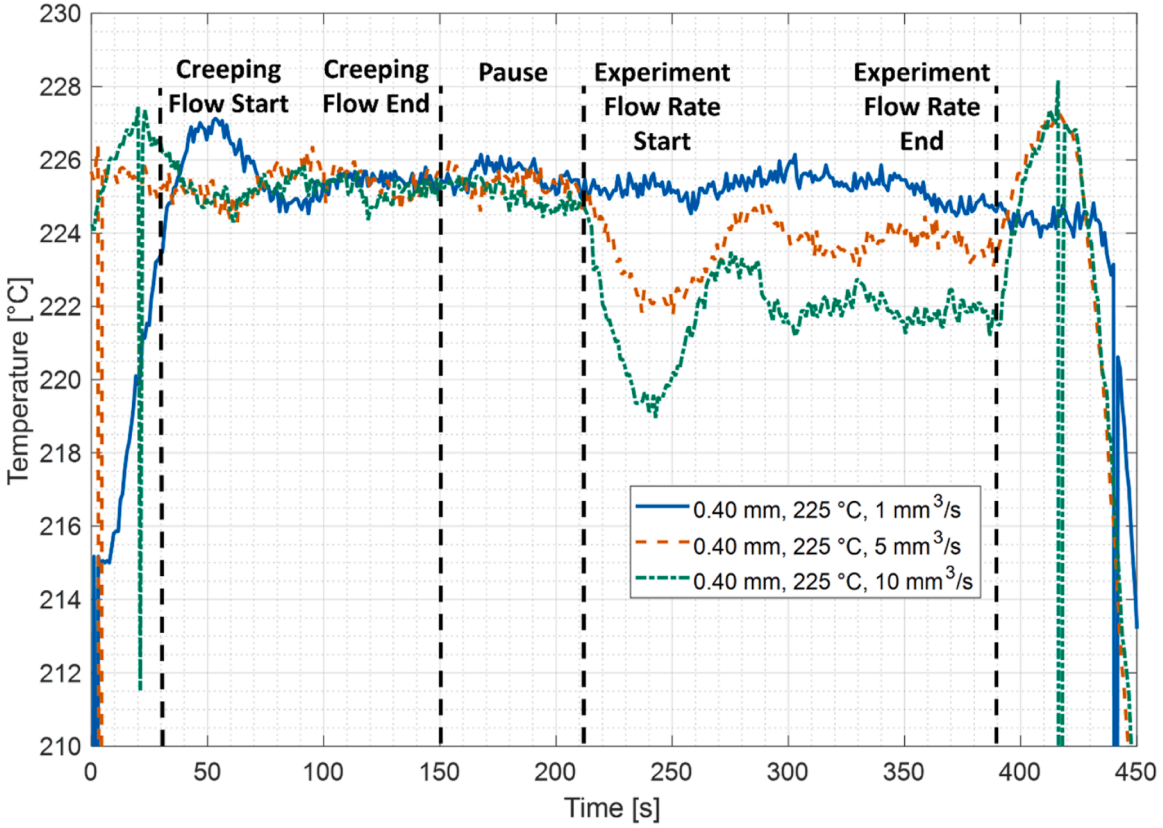

Fig. 10. Transient measured temperature data for a nozzle diameter of 0.40 mm and a temperature setpoint of 225 °C.

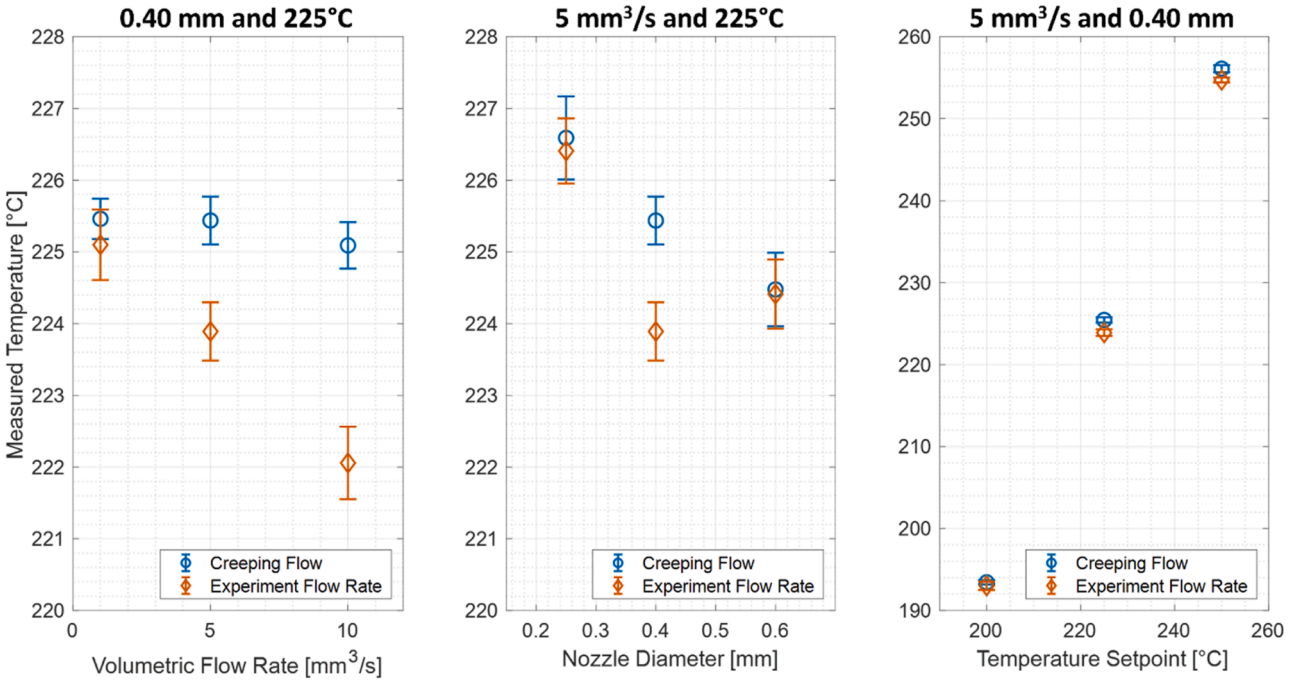

Fig. 11. Measured temperature versus the factors. The data points are average values and the error bars represent one standard deviation.

torque sensor produces the greatest pressure estimate because it is the closest to the motor and there will be frictional losses in the gearing, feed tube, inlet to the hot end, melting channel of the hot end, and nozzle. The torque sensor reading decaying slower than the other two sensors was unexpected but may suggest that the solid filament is compressed by the driven gear when extrusion ends, resulting in the torque remaining at a nonzero value until the filament is removed or extrusion begins again. Alternatively, the bearings for the gears and shafts may have friction that requires movement to release residual forces. The infeed sensor readings observed between the direct melt pressure and the

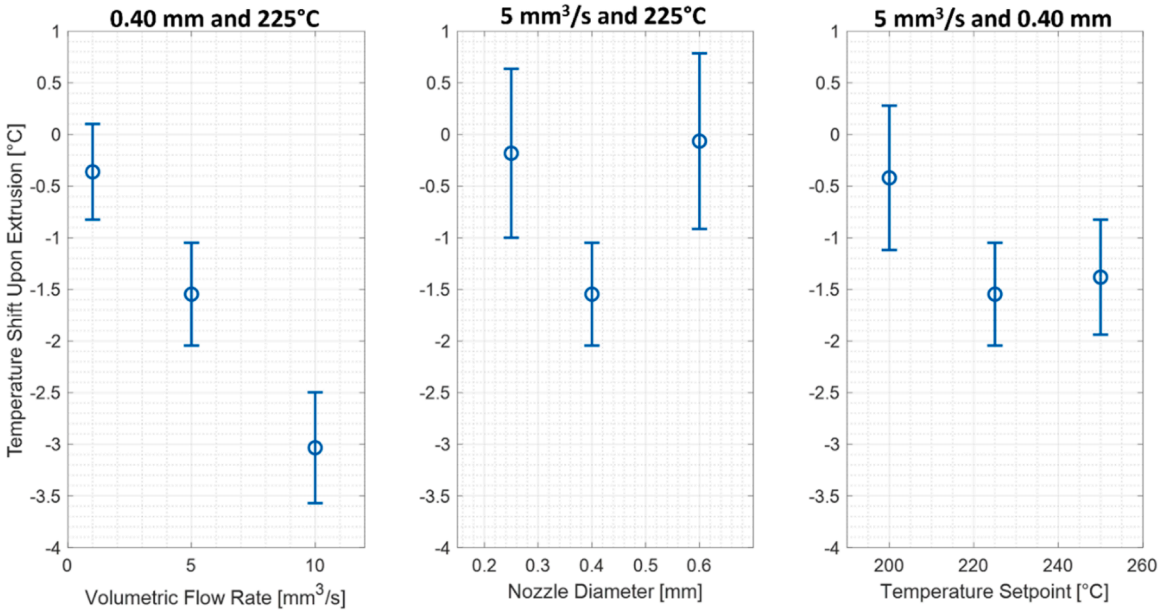

Fig. 12. Temperature shift upon extrusion versus the factors. The data points are average values and the error bars represent one standard deviation.

torque sensor are expected as well because there is material between the infeed sensor and the other two.

The variations in the signals across the sensing techniques is an important indicator of the variations in flow rate that may affect all gear-driven material extrusion processes. Fig. 13 plots the first 22 s of the sensor readings for the center point of the experiment design (run 1 of Table 3 with a flow rate of 5 mm^3/s); the added symbols are solely for trace identification. The observed high frequency pulses correspond to the 17 discrete gear teeth engaging the filament. Specifically, the gear pitch diameter is 7.75 mm and corresponds to a driven filament length of 24.35 mm per gear turn. For a filament diameter of 1.75 mm, this driven length corresponds to a volumetric displacement of 58.5 mm^3 per gear turn. Across the 22 s of Fig. 13, approximately 110 mm^3 of material will be extruded at a flow rate of 5 mm^3/s. This extruded volume corresponds to about two turns of the drive gears. Direct inspection (counting of the 38 high frequency peaks) shows that they directly correspond to the engagement of the filament by the 17 teeth during each full rotation of the gears. These high frequency pulses can be

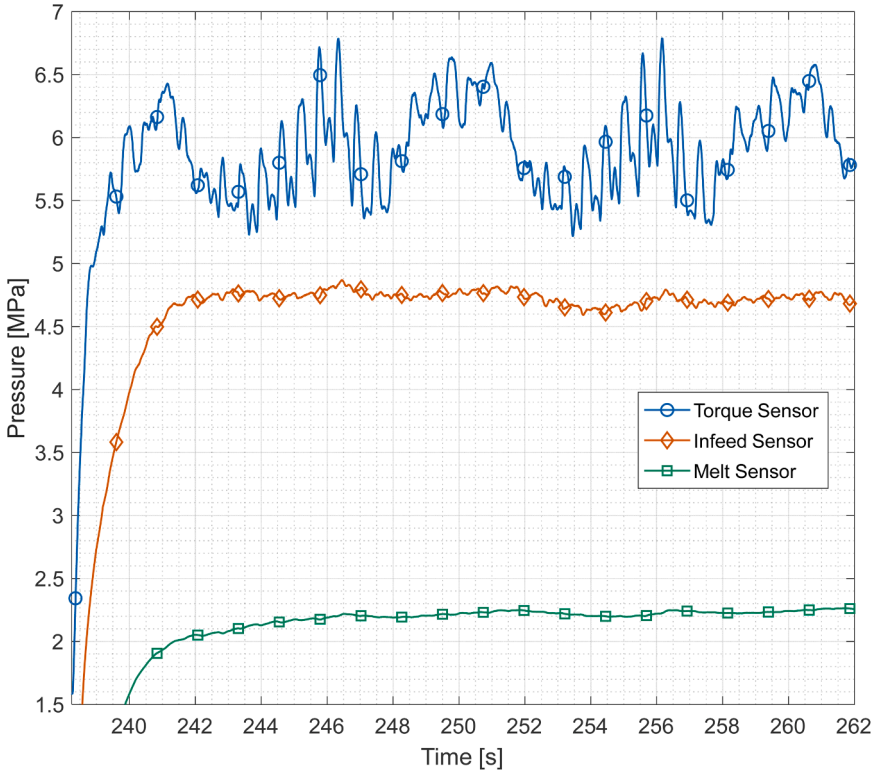

Fig. 13. Pressure versus time for 0.40 mm nozzle orifice diameter, 225 °C temperature setpoint and 5 mm^3/s volumetric flow rate for a few rotations of the extruder gear.

transmitted to the infeed load sensor and (depending upon the process conditions, magnitude of variation, and material rheology) can also be transmitted to the melt pressure in the hot end as reported by [11] and clearly shown in the left subplot of Fig. 6, among others.

While the high frequency variation is concerning, even more concerning is the low frequency behavior. The source of these low frequency variations is the eccentricity of the drive gear on the driven D-shafts. Specifically, a sliding fit clearance, typically on the order of 0.1 mm for a 5 mm shaft diameter allows for ease of assembly of the gear onto the D-shaft. The angular position of the gear is then fixed using a secured set screw pressing against the flat on the D-shaft and driving eccentricity of the drive gear. Given the gear pitch of 7.75 mm, an eccentricity of 0.1 mm would mean that the flow rate varies in a sinusoidal fashion with an amplitude of 2.6% (0.1/7.75) with every rotation of the drive gears. This low frequency variation is transmitted to the melt in the hot end and is a root cause of variation in all gear-driven material extrusion processes. The analysis in the prior paragraph indicates that the drive gears rotate twice, yet four low frequency peaks are clearly observed in Fig. 13; this behavior indicates that the two gears are oriented so that the flats on their D-shafts are nearly 90° out of phase. The magnitude of low frequency variation will change based on the gear design and relative orientation (and resulting phase angle) between the driving and driven gear. To reduce the low frequency variation, tighter fits or press fitting the drive gears to the driven shafts is recommended.

The temperature varying as a function of volumetric flow rate is expected, as the increasing flow rate transports more material at ambient temperature into the hot end, resulting in a decreased melt temperature. It is also expected that the temperature would equilibrate at a value between the initial lower temperature and the original temperature once the volumetric flow rate reaches steady state. For the 0.25 mm and 0.60 mm nozzle orifice diameters, the temperature remains stable when the extruder performs the experiment flow rate. This may be due to pressure work counteracting the influx of ambient temperature material for the 0.25 mm nozzle. For the 0.60 mm nozzle orifice diameter, the temperature of the material is already slightly lower than the setpoint during the creeping flow and it stays at that temperature during the commanded volumetric flow rate. This behavior is likely due to the shear stress required to extrude the material through this orifice at the volumetric flow rates prescribed being lower than the shear stress in the other nozzle orifices, making it easier for the hot material to flow out and the cold material to flow in. For the temperature shift as a function of temperature setpoint, the higher of the two temperature setpoints show greater decreases in the temperature for the same nozzle orifice diameter and volumetric flow rate. This greater temperature shift is likely due the rate of convective heat transfer being proportional to the temperature gradient, meaning the greater the difference between the temperature setpoint and ambient temperature (the temperature of the material being fed into the hot end), the greater the rate of heat transfer from the material in the hot end to the material entering the hot end. This phenomenon leads to a greater decrease in temperature at higher temperature setpoints.

Looking at the signals from the three different sensors, the melt pressure and melt temperature are likely most valuable because they are directly adjacent to the melt and indicative of the process states in situ. However, these sensors require a custom hot end design, not only increasing its mass but also potentially affecting the process, e.g., due to heat conduction. The torque sensor, on the other hand, exhibits excellent sensitivity and is the least invasive, but the data is far removed from the processed melt. The infeed load sensor provides a compromise between the other two sensors. It is closer to the melt than the torque sensor and does not disturb the flow of the polymer, but is also less indicative of the process states in the nozzle. Currently, infeed load sensors are being adopted and are certainly better than nothing for quality assurance. We believe that high temperature piezoelectric and ultrasonic sensors located in the hot end or nozzle are likely to provide more compact, less invasive, and high-quality solutions in the future.

6. Conclusions

These experiments show that the pressure required to extrude ABS in thermoplastic material extrusion additive manufacturing increases with volumetric flow rate and decreases with nozzle orifice diameter and temperature setpoint, consistent with processing theory. The pressure measured by the shaft torque sensor is shown to always be greater than the pressure measured by the infeed load and melt pressure sensors, and the infeed load pressure is always shown to be greater than the melt pressure. The torque sensor is observed to have the greatest variation out of the three, due to its sensitivity to the extruder gear geometry and assembly. Additionally, the pressure loss in the melt, between the infeed and melt sensors, is found to increase as a function of volumetric flow rate and nozzle orifice diameter, and decrease as a function of the temperature setpoint. The COMSOL model is shown to estimate the trends observed in the melt pressure well for all factors, despite underpredicting the experimental values. The Poiseuille model underpredicts the melt pressure due to isothermal and Newtonian flow assumptions.

The melt temperature is found to vary as a function of the volumetric flow rate and the temperature setpoint, but not the nozzle diameter, which are all expected results. The decrease in melt temperature likely contributes to greater increases in the pressure with volumetric flow rate, since the viscosity will be higher at lower temperatures. Overall, this work shows how the pressure and behavior at the stepper motor affect the pressure downstream, that the pressure and flow are sensitive to the extruder configuration, and that the melt pressure sensor provides the clearest estimation of the rheological state within the hot end. Care should be taken in selecting and mounting drive gears to minimize low and high frequency variation respectively due to gear eccentricity and teeth-to-filament engagement.

CRediT authorship contribution statement

David O. Kazmer: Writing – review & editing, Visualization, Supervision, Software, Resources, Project administration, Methodology, Investigation, Funding acquisition, Formal analysis, Conceptualization. **Austin Colon:** Writing – original draft, Visualization, Validation, Software, Methodology, Investigation, Formal analysis, Data curation, Conceptualization. **Amy M. Peterson:** Writing – review & editing, Supervision, Resources, Project administration, Methodology, Investigation, Funding acquisition, Conceptualization.

Declaration of Competing Interest

The authors declare that they have no known competing financial interests or personal relationships that could have appeared to influence the work reported in this paper.

Data Availability

The data is available via a DOI in the manuscript.

Acknowledgements

This work is supported by the National Science Foundation (NSF) under. GOALI Grant No. #1914651. Any opinions, findings, and conclusions or recommendations expressed in this material are those of the author(s) and do not necessarily reflect the views of the NSF. The authors also acknowledge Stratasys, Ltd. as the University of Massachusetts (UMass) Lowell team's GOALI partner. Additionally, the authors acknowledge the National Institute of Standards of Technology for providing the nozzles used in the experiments. Lastly, the first author thanks David Rondeau, the technician at UMass Lowell, for his assistance and guidance in machining the hot end and other components.

Declaration of competing interest

The authors declare no competing interests. One of the authors of this article is part of the Editorial Board of the journal. To avoid potential conflicts of interest, the responsibility for the editorial and peer-review process of this article lies with the journal's other editors. Furthermore, the authors of this article were removed from the peer review process and had no, and will not have, any access to confidential information related to the editorial process of this article.

Supplemental materials

Supplemental materials provide further details on the data acquisition system, material properties, estimation of the Nusselt number, thermal contact resistance modeling, and torque characterization. The data from the experiments is currently available at: https://doi.org/10.18126/FU80-S9BT.

Appendix A. Supporting information

Supplementary data associated with this article can be found in the online version at doi:10.1016/j.addma.2023.103780.

References

[1] Krishnanand, S. Soni, M. Taufik, Design and assembly of fused filament fabrication (FFF) 3D printers, Mater. Today.: Proc. 46 (2021) 5233–5241.
[2] B. N. Turner, R. Strong, S. A. Gold, A review of melt extrusion additive manufacturing processes: I. Process design and modeling, Rapid Prototyp. J. 20 (3) (2014) 192–204.
[3] S. Singh, et al., Current status and future directions of fused filament fabrication, J. Manuf. Process. 55 (2020) 288–306.
[4] M. Salmi, Additive manufacturing processes in medical applications, Materials 14 (1) (2021) 191.
[5] H. Klippstein, et al., Fused deposition modeling for unmanned aerial vehicles (UAVs): a review, Adv. Eng. Mater. 20 (2) (2018).
[6] E. Garcia Plaza, et al., Analysis of pla geometric properties processed by FFF additive manufacturing: effects of process parameters and plate-extruder precision motion, Polymers 11 (2019).
[7] T. Beran, et al., Nozzle clogging factors during fused filament fabrication of spherical particle filled polymers, Addit. Manuf. 23 (2018) 206–214.
[8] C. Luo, et al., Effects of feed rates on temperature profiles and feed forces in material extrusion additive manufacturing, Addit. Manuf. 35 (2020).
[9] J. Go, et al., Rate limits of additive manufacturing by fused filament fabrication and guidelines for high-throughput system design, Addit. Manuf. 16 (2017) 1–11.
[10] C. Luo, et al., Upper bound of feed rates in thermoplastic material extrusion additive manufacturing, Addit. Manuf. 32 (2020).
[11] D.O. Kazmer, et al., Concurrent characterization of compressibility and viscosity in extrusion-based additive manufacturing of acrylonitrile butadiene styrene with fault diagnoses, Addit. Manuf. 46 (2021).
[12] M.E. Mackay, The importance of rheological behavior in the additive manufacturing technique material extrusion, J. Rheol. 62 (6) (2018) 1549–1561.
[13] M.H. Khaliq, et al., On the use of high viscosity polymers in the fused filament fabrication process, Rapid Prototyp. J. 23 (4) (2017) 727–735.
[14] A. Das, et al., Importance of polymer rheology on material extrusion additive manufacturing: correlating process physics to print properties, ACS Appl. Polym. Mater. 3 (3) (2021) 1218–1249.
[15] C. Duty, et al., What makes a material printable? A viscoelastic model for extrusion-based 3D printing of polymers, J. Manuf. Process. 35 (2018) 526–537.
[16] S.K. Kim, et al., Non-Newtonian modeling of contact pressure in fused filament fabrication, J. Rheol. 65 (1) (2021) 27–42.
[17] T.J. Coogan, D.O. Kazmer, Prediction of interlayer strength in material extrusion additive manufacturing, Addit. Manuf. 35 (2020).
[18] M.P. Serdeczny, et al., Viscoelastic simulation and optimisation of the polymer flow through the hot-end during filament-based material extrusion additive manufacturing, Virtual Phys. Prototyp. 17 (2) (2022) 205–219.
[19] M. Moretti, A. Rossi, N. Senin, In-process simulation of the extrusion to support optimisation and real-time monitoring in fused filament fabrication, Addit. Manuf. 38 (2021).
[20] J. Chen, D.E. Smith, Filament rheological characterization for fused filament fabrication additive manufacturing: a low-cost approach, Addit. Manuf. 47 (2021).
[21] J. Fischer, et al., In-line measurement of extrusion force and use for nozzle comparison in filament based additive manufacturing, Prog. Addit. Manuf. (2023).
[22] M.P. Serdeczny, et al., Experimental and analytical study of the polymer melt flow through the hot-end in material extrusion additive manufacturing, Addit. Manuf. 32 (2020).
[23] V. Nienhaus, et al., Investigations on nozzle geometry in fused filament fabrication, Addit. Manuf. 28 (2019) 711–718.
[24] W. De Backer, et al., In-process monitoring of continuous fiber additive manufacturing through force/torque sensing on the nozzle, AIAA Scitech 2020 Forum (2020).
[25] G.A. Mazzei Capote, et al., Trends in force and print speed in Material Extrusion, Addit. Manuf. 46 (2021).
[26] T.J. Coogan, D.O. Kazmer, In-line rheological monitoring of fused deposition modeling, J. Rheol. 63 (1) (2019) 141–155.
[27] D.A. Anderegg, et al., In-situ monitoring of polymer flow temperature and pressure in extrusion based additive manufacturing, Addit. Manuf. 26 (2019) 76–83.
[28] Y. Tlegenov, W.F. Lu, G.S. Hong, A dynamic model for current-based nozzle condition monitoring in fused deposition modelling, Prog. Addit. Manuf. 4 (3) (2019) 211–223.
[29] S.K. Michael Simpson, Inexpensive piezoelectric elements for nozzle contact detection and build platform leveling in FFF 3D printers, Inventions 3 (1) (2018).
[30] J.E. Seppala, K.D. Migler, Infrared thermography of welding zones produced by polymer extrusion additive manufacturing, Addit. Manuf. 12 (2016) 71–76.
[31] E. Ferraris, J. Zhang, B. Van Hooreweder, Thermography based in-process monitoring of fused filament fabrication of polymeric parts, CIRP Ann. 68 (1) (2019) 213–216.
[32] Y. Li, et al., In-situ monitoring and diagnosing for fused filament fabrication process based on vibration sensors, Sensors 19 (11) (2019).
[33] W. Lin, et al., Online quality monitoring in material extrusion additive manufacturing processes based on laser scanning technology, Precis. Eng. 60 (2019) 76–84.
[34] A. Bellini, Su Güç¸eri, M. Bertoldi, Liquefier dynamics in fused deposition, J. Manuf. Sci. Eng. 126 (2) (2004) 237–246.
[35] D.D. Phan, Z.R. Swain, M.E. Mackay, Rheological and heat transfer effects in fused filament fabrication, J. Rheol. 62 (5) (2018).
[36] T.A. Osswald, J. Puentes, J. Kattinger, Fused filament fabrication melting model, Addit. Manuf. 22 (2018) 51–59.
[37] G. Percoco, et al., Analytical model to predict the extrusion force as a function of the layer height, in extrusion based 3D printing, Addit. Manuf. 38 (2021).
[38] E.L. Gilmer, et al., Model analysis of feedstock behavior in fused filament fabrication: enabling rapid materials screening, Polymer 152 (2018) 51–61.
[39] Y. Tlegenov, Y.S. Wong, G.S. Hong, A dynamic model for nozzle clog monitoring in fused deposition modelling, Rapid Prototyp. J. 23 (2) (2017) 391–400.
[40] J.L. Colón Quintana, et al., Implementation of shear thinning behavior in the fused filament fabrication melting model: Analytical solution and experimental validation, Addit. Manuf. 37 (2021).
[41] D.D. Phan, et al., Computational fluid dynamics simulation of the melting process in the fused filament fabrication additive manufacturing technique, Addit. Manuf. 33 (2020).
[42] S. Marion, et al., First steps of the melting of an amorphous polymer through a hot-end of a material extrusion additive manufacturing, Addit. Manuf. 65 (2023).
[43] F. Pigeonneau, et al., Heating and flow computations of an amorphous polymer in the liquefier of a material extrusion 3D printer, Addit. Manuf. 32 (2020).
[44] C.O. Ufodike, G.C. Nzebuka, Investigation of thermal evolution and fluid flow in the hot-end of a material extrusion 3D Printer using melting model, Addit. Manuf. 49 (2022).
[45] G.C. Nzebuka, et al., Numerical modeling of the effect of nozzle diameter and heat flux on the polymer flow in fused filament fabrication, J. Manuf. Process. 82 (2022) 585–600.
[46] M.P. Serdeczny, et al., Numerical modeling of the polymer flow through the hot-end in filament-based material extrusion additive manufacturing, Addit. Manuf. 36 (2020).
[47] J. Kattinger, et al., Numerical simulation of the complex flow during material extrusion in fused filament fabrication, Addit. Manuf. 49 (2022).
[48] A.M. Peterson, Review of acrylonitrile butadiene styrene in fused filament fabrication: a plastics engineering-focused perspective, Addit. Manuf. 27 (2019) 363–371.
[49] T. Osswald, N. Rudolph, Generalized newtonian fluid models. in *Polymer Rheology - Fundamentals and Applications*, Hanser Publications, Cincinnati, Ohio, 2014, pp. 59–97.
[50] C. O'Carroll, K.S. Sorbie, Generalization of the Poiseuille law for one- and two-phase flow in a random capillary network, Phys. Rev. E Stat. Phys. Plasmas Fluids Relat. Inter. Top. 47 (5) (1993) 3467–3476.
[51] T. Van Waeleghem, et al., Melt exit flow modelling and experimental validation for fused filament fabrication: From Newtonian to non-Newtonian effects, J. Manuf. Process. 77 (2022) 138–150.
[52] T.J. Coogan, D.O. Kazmer, Bond and part strength in fused deposition modeling, Rapid Prototyp. J. 23 (2) (2017) 414–422.
[53] T. Tezel, V. Kovan, Determination of optimum production parameters for 3D printers based on nozzle diameter, Rapid Prototyp. J. 28 (1) (2021) 185–194.
[54] Deen, W.M., ed. *Analysis of Transport Phenomena*. 2nd ed. 2012, Oxford University Press.
[55] H.W. Cox, C.W. Macosko, Viscous dissipation in die flows, AIChE J. 20 (4) (1974) 785–795.
[56] Y.A. Cengel, J.M. Robert, R.H. Turner, in: B. Stenquist. (Ed.), Fundamentals of Thermal-Fluid Sciences, fourth ed., McGraw-Hill, New York, 2012.
[57] H. Massé, et al., Heat transfer with mechanically driven thermal contact resistance at the polymer–mold interface in injection molding of polymers, Int. J. Heat. Mass Transf. 47 (8–9) (2004) 2015–2027.